Identification of Diffusion Transport Properties from Desorption/Sorption Kinetics: An Analysis Based on a New Approximation of Fick Equation during Solid−Liquid Contact

Olivier Vitrac*,† and Murielle Hayert‡

UMR Fractionnement des Agro-Ressources et Emballage, INRA 614, Moulin de la Housse, 51687 Reims Cedex 2, France, and UMR Génie des Procédés Environnement et Agro-alimentaire, CNRS 6144, ENITIAA, La Géraudière, 44322 Nantes Cedex 3, France

The identifiability of three diffusion properties (diffusion coefficient D, partition coefficient K, and convective mass transfer coefficient h_m) from desorption kinetics (or equivalently sorption kinetics) was investigated from a new approximated analytical solution of 1D diffusion coupled with a Robin boundary condition. A generalized least-squares criterion, which extends classical identification techniques, was proposed. The robustness of classical and modified criteria was compared on both experimental and simulated data including different sampling strategies and noise levels. Confidence intervals and bias were calculated for a large set of conditions: desorption levels ranged between 30% and 100% (equilibrium), the dilution factor ranged between 10^{-3} and 10^{-1}, mass Biot numbers ranged between 10^{-1} and 10^{4}, and the K value ranged between 10^{-3} and 5.

1. Introduction

Diffusion transport of solutes, reactants, or pollutants between a solid and a fluid phase has major importance in many scientific and technological areas and has been extensively studied from the experimental point of view.[1−3] Conventionally, the different properties that control the sorption or desorption rate (diffusion coefficient in the solid phase, D; partition coefficient between both phases, K; and interfacial mass transfer coefficient, h_m) have been estimated from independent experiments so that internal, interfacial, and thermodynamical phenomena may be separated.[4,5] This work analyzes the identifiability and identification of several diffusion properties $p = [D,K,h_m]'$ from a single desorption/sorption kinetic, which may be subjected to physical constraints. This work is motivated by the need to achieve standard diffusion coefficients of additives and monomers in plastic materials when they are put in contact with food simulants. These diffusion coefficients can be used subsequently to test the compliance of food contact materials as acknowledged by the EU Directive 2002/72/EC[6] or to perform a priori sanitary surveys of food contact materials.[7]

Two generic constraints are considered: (i) when the macroscopic thermodynamic equilibrium is not reached (incomplete sorption/desorption kinetics) and (ii) when a significant contribution of interfacial mass transport resistances is expected. The first situation occurs when the final equilibrium desorption/sorption state is either not observed or nonobservable (e.g., because of prohibitive diffusion time, material aging, uncontrolled mass losses, or reactions). The second situation is met when the diffusant has a low chemical affinity for the liquid phase (thermodynamical limitation of mass transfer) and/or when the mass transfer resistance in the fluid phase is significant consequent to the viscosity of the fluid phase or consequent to the large resistance to the diffusion encountered in the solid phase (e.g., very thick materials or very low diffusion coefficients). Falsely neglecting thermodynamic and external mass transfer contributions, when they are not negligible, leads to a significant overestimation of the internal mass transport resistance in the solid phase and, therefore, to a significant underestimation of the "true" diffusion coefficient in the solid phase (D). Such a bias in D estimation may yield erroneous conclusions if the value is included within a database, used for the optimization of either a process or a formulation, or used for regulation purposes.

The identification of the unknown vector of parameters, p, from desorption or sorption kinetic data is commonly obtained by minimizing iteratively a merit function $\chi^2(p)$ that assesses the closeness of experimental data (e.g., average concentration either in the solid phase or in the fluid phase) to simulated ones. A maximum likelihood estimator, $\hat{p}$, is intuitively assumed to exist, to be unique, and to occur when the minimum of $\chi^2(p)$ is reached. In practice, the identification of several properties from nonoptimally designed experiments may fail or may lead to unreliable results.[8] Indeed, this approach assumes implicitly (i) that the system is identifiable and (ii) that the measurement errors are independent and identically distributed with zero mean. In particular, when errors do not fulfill such a hypothesis (e.g., because of data including colored noise or correlations), uncertainty increases drastically and least-squares estimators are biased.[9−11]

The paper is organized as follows. The issue of feasibility of the simultaneous identification of three properties from a single desorption/sorption kinetic is theoretically discussed in Section 2. The analysis is based on a novel algebraic solution of the general dimensionless 1D mass transport problem governing the desorption/sorption kinetic. The original partial differential equation (PDE) describing the mass transport problem is replaced by an algebraic differential equation (DAE) describing the trajectory of the sole measurable quantity. As a result, the evolution of the concentration either in the solid or in the liquid phase is described in a new approximation space, called kinetic phase diagram (KPD), where the concentration value at equilibrium can be more easily extrapolated and where the contributions of internal and external mass transfer resistances can be more easily distinguished.

The rest of the work presents identification results on practical cases based on on both experimental and simulated data. The

* Corresponding author. Tel.: +33(0)326918572. Fax: +33(0)326913916. E-mail: olivier.vitrac@reims.inra.fr.

† UMR Fractionnement des Agro-Ressources et Emballage.

‡ UMR Génie des Procédés Environnement et Agro-alimentaire.

10.1021/ie060347w CCC: $33.50
Published on Web 00/00/0000 **PAGE EST: 15.3**

performances of both the standard criterion, $\chi^2(p)$, and the generalized least-squares criterion derived from KPD, $\chi^{2*}(p)$, are tested in terms of bias and uncertainty. Section 3 briefly presents experimental conditions that were used to monitor almost continuously the diffusion of a UV tracer from a suspension of low-density polyethylene to different food simulants. Since a time differentiation of the concentration is required for KPD, a robust nondeterministic differentiation technique of kinetic data is also presented. Section 4 discusses the global performance of both criteria from experimental data. Section 5 presents a detailed sensitivity analysis of both strategies for a large set of training data corresponding to different desorption rates (from 30% to 100% of the equilibrium value), sampling strategies, and mass Biot values. The conclusions and a general discussion on the conditions that can be practically used to identify three diffusion transport properties from a single desorption/sorption kinetic follow in Section 6.

2. Theoretical Section: The Forward Problem and Its Approximation

This section describes the unsteady diffusion of a species from a solid phase toward a fluid phase (desorption kinetic) when no reaction and interaction (plasticization, swelling) occur between the solid and a liquid. The reverse transport corresponding to the sorption case is not presented but it can be easily extended from presented results. The solid phase is noted S. The fluid phase is noted L because it is envisioned mainly as a liquid, but the boundary and thermodynamic conditions are generic enough to be also valid for gaseous phases. The system S + L is assumed to be closed (no mass losses or gains).

2.1. Dimensionless Transport and Mass Balance Equations. Assuming 1-dimensional transport (the side effects are negligible), a constant diffusion coefficient (D), and a constant S-phase thickness, the dimensionless mass transport equation is

$$\frac{\partial u}{\partial \theta} = \frac{\partial^2 u}{\partial x^{*2}} \tag{1}$$

where $u = (C_S(x,t)/C_S^0)$, $x^* = (x/l_S)$, and $\theta = (tD/l_S^2)$ are, respectively, the dimensionless concentration, position, and time (so-called Fourier time). C_S^0 is a strictly positive constant. Consistently, the concentrations C_S and C_S^0 are concentrations per unit of volume. l_S is either the whole or half thickness of the solid material, depending on the type of contact with the L phase, respectively, single- or double-sided.

The S−L interface is located at $x^* = 1$. At this interface, the local thermodynamical equilibrium is assumed. The desorption and sorption are assumed to be reversible in each phase and controlled by a an equilibrium relationship similar to Henry's law.[12,13] This condition is generally well-verified for diffusants distributed at low concentrations in dense phases, fluid phases, or a combination of both.[14] This description entails a possible discontinuous concentration at the S−L interface. The ratio of concentration on both sides of the interface defines the partition coefficient between both phases: $K = (C_L(x^* = 1^+, t)/C_S(x^* = 1^-, t))$, where $C_L(x^*, t)$ is the local concentration in the L phase.

In the L phase, a combination of molecular diffusion and convection is assumed. Diffusion is assumed to dominate close to the S−L interface, where the fluid velocity is the lowest, while inertia forces due to natural or forced convection are assumed to control the dispersion of the diffusing species elsewhere. Since only concentration gradients are expected near the S−L interface, the mass flux at the interface is controlled by a mass transfer coefficient, h_m, with SI units in $m \cdot s^{-1}$, whereas a uniform concentration $Ku|_{x^* \to \infty}$ exists far from the S−L interface. The corresponding dimensionless boundary condition (BC) is written as a Robin BC detailed in eq 2. A similar equation was derived by Gandek et al.[15]

$$j^* = -\left.\frac{\partial u}{\partial x^*}\right|_{x^*=1} = BK(u|_{x^*=1} - u|_{x^* \to \infty}) \tag{2}$$

where $j^* = (l_S/DC_S^0)\, j$ is a dimensionless flux and j is the interfacial mass flux density (with SI units in $kg \cdot m^{-2} \cdot s^{-1}$). $B = (R_D/R_H) = (h_m l_S/D)$, the so-called mass Biot number, is the ratio between the equivalent resistance to diffusion in the solid phase, R_D, and the mass transport resistance at the S−L interface, R_H.

$Ku|_{x^* \to \infty}$ stands for the concentration on the liquid side far from the S−L interface. When the concentration is homogeneous far from the S−L interface (i.e., when the volume of the boundary layer is assumed to be negligible compared to the volume of L), it is conveniently approximated by the concentration in the bulk, as it would be measured in L. Both descriptions are almost equivalent when the transport property in L is much greater than the transport property in P (the case of most liquids) or when a mixing process (e.g., convection) occurs on the L side. The diffusant mass balance between S and L phases between times 0 and θ leads to the following approximation for $u|_{x^* \to \infty}$,

$$u|_{x^* \to \infty} = u|_{x^* \to \infty}^{\theta=0} + \frac{1}{K} \cdot \frac{1}{C_S^0} \cdot \frac{1}{l_L} \cdot \int_0^t j(\tau)\, d\tau = u|_{x^* \to \infty}^{\theta=0} + \frac{1}{K} L^* \int_0^\theta j^*(\tau)\, d\tau \tag{3}$$

where $Ku|_{x^* \to \infty}^{\theta=0}$ is the initial concentration in the L phase, assumed to be uniform. $l_L = (S_{SL}/V_L)$ is the characteristic dimension of the liquid reservoir of volume V_L and with a surface contact area with S noted S_{SL}. $L^* = (l_S/l_L)$ is a dimensionless length and characterizes the typical relative distance that a diffusant initially in the S phase must cross before migrating into the L phase. When the volume of the liquid region subjected to to a concentration gradient is no longer negligible (e.g., when $L^* \xrightarrow{>} 1$), $u|_{x^* \to \infty}$ must preferably be inferred by introducing a transport equation for the liquid phase. If not, the use of the average concentration in L, defined by eq 3, instead of the concentration far from the interface (in the bulk), modifies the commonly accepted definition of the mass transport coefficient, h_m, in eq 2. In the rest of the work, the volume of the boundary layer is assumed to be not limiting.

Equation 2 combined with eq 3 yields the practical form of the BC, written here as an integro-differential operator:

$$j^* = -\left.\frac{\partial u}{\partial x^*}\right|_{x^*=1} = BK(u|_{x^*=1} - u|_{x^* \to \infty}^{\theta=0}) - BL^* \int_0^\theta j^*(\tau)\, d\tau \tag{4}$$

Two extreme cases are derived from eq 4 by assuming (i) $R_H = 0$ (i.e., no limiting mass transfer boundary layer), (ii) $K/L^* \to \infty$.

Case (i) is inferred by differentiating eq 3 with time for $u|_{x=1} = u|_{x \to \infty}$:

$$\frac{\partial u|_{x^*=1}}{\partial \theta} = \frac{L^*}{K} j^* = -\frac{L^*}{K} \left.\frac{\partial u}{\partial x^*}\right|_{x^*=1} \tag{5}$$

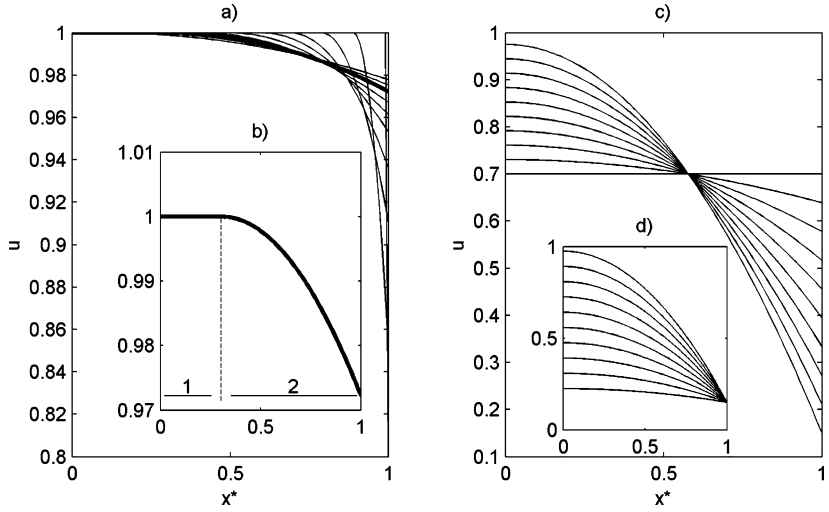

Figure 1. Parabolic approximations of internal concentration profiles for $u(x^*,\theta = 0) = 1$: (a) examples of approximation by a piecewise second-degree polynomials in case of a short time S−L contact and the same residual concentration $\bar{u}$; (b) details of the profile in bold line (region 1, $u = 1$; region 2, $(\partial^2 u/\partial x^{*2}) = C^{te}$); (c) examples of approximation by single second-degree polynomials in case of long time S−L contact and the same value of $\bar{u}$; (d) idem for the same value of $u(x^* = 1)$.

Table 1. Values of α and j^*_R Defined in Equation 12 for Particular Conditions on Parameters *K*, *B*, and *L** **(Assuming Fully Developed Parabolic Profiles)**

reduced condition	α	j^*_R	$\bar{u}\|_{t\to\infty} = \frac{j^*_R}{\alpha}$
$K \to \infty$	3	$3u\|^{\theta=0}_{x^*\to\infty}$	$u\|^{\theta=0}_{x^*\to\infty}$
$K \to 0$	BL^*	$BL^*u\|_{\theta=0}$	$\bar{u}\|_{\theta=0}$
$L^* \to 0$	$\frac{BK}{1+\frac{1}{3}\cdot BK}$	$\frac{BKu\|^{\theta=0}_{x^*\to\infty}}{1+\frac{1}{3}BK}$	$u\|^{\theta=0}_{x^*\to\infty}$
$B \to \infty$	$3\left(1+\frac{L^*}{K}\right)$	$3\left(\frac{L^*}{K}\bar{u}\|_{\theta=0} + u\|^{\theta=0}_{x^*\to\infty}\right)$	$\frac{L^*\bar{u}\|_{\theta=0} + Ku\|^{\theta=0}_{x^*\to\infty}}{K+L^*}$
$B \to 0$	$B(K+L^*)$	$B(L^*\bar{u}\|_{\theta=0} + Ku\|^{\theta=0}_{x^*\to\infty})$	$\frac{L^*\bar{u}\|_{\theta=0} + Ku\|^{\theta=0}_{x^*\to\infty}}{K+L^*}$

By analogy with wave propagation equations, eq 5 is known as a reflecting boundary condition, where the amount of matter that leaves the S−L interface modifies in return (i.e., after accumulation or "reflection") the mass transfer resistance at the interface. K/L^* is the equivalent dimensionless "reflecting distance", where the quantity K is similar to a dimensionless "absorbing" coefficient.

Case (ii) corresponds to a very large volume of L ($L^* \to 0$) or capacity ($K \to \infty$) in BC defined by eq 2, that is, $(\partial u|_{x^*=1}/\partial\theta) \to 0$ or the equivalent Dirichlet's BC:

$$u|^{(\theta)}_{x^*=1} = u|^{(\theta=0)}_{x^*=1} \tag{6}$$

For the left-side boundary, $x^* = 0$, an impervious, or equivalently a symmetry, BC is applied:

$$\left.\frac{\partial u}{\partial x^*}\right|_{x^*=0} = 0 \tag{7}$$

2.2. Formulation of Kinetic Phase Diagrams (KPDs). In its general form, the partial differential equation (PDE), defined by eq 1, combined with an initial condition (IC) $u(x^*, \theta = 0)$ and BCs defined by eq 4 and 7 has no exact analytical solution.[16] Particular solutions must be approximated (i) via a numerical resolution with low- or high-order spectral techniques or (ii) via a local decomposition of the solution as an expansion series on a suitable basis of analytical eigenfunctions. A general solution as an expansion series is detailed by Sagiv.[3] Practically, such calculations have severe inherent drawbacks that limit their use in efficient nonlinear identification algorithms:

(i) They are time-consuming (specially for numerical resolution).

(ii) They require tables of eigenvalues and weighting coefficients (especially for expansion series).[3]

(iii) They do not provide any explicit relationships between physical parameters (e.g., D, K, and h_m), geometrical parameters (e.g., l_S, l_L, and x), kinetic parameters (t), and measurements (e.g., residual concentration in S, accumulated concentration in L, and flux j).

(iv) They cannot be easily extended for boundary conditions that are variable in time (especially for expansion series).

To overcome such difficulties, a general alternative formulation based on polynomial approximation of the concentration in S is described. This approach is introduced to provide an analytical expression of the dimensionless KPD, $j^* = f(\bar{u})$, where $\bar{u}$ is the residual concentration in the S phase. The demonstration is focused on the main relevant IC and BC for conventional applications, which are $u(x^*, \theta = 0) = 1$ (e.g., uniform distribution of the diffusant) and the general BC defined in eq 4. In addition, the expression of $j^* = f(\bar{u})$ (eqs 12 and 16) is also valid when external conditions are variable with time. The calculated solution thus provides a suitable state equation for algorithms that aim to control mass transport according to kinetic or thermodynamic constraints and subjected to external perturbations.

D

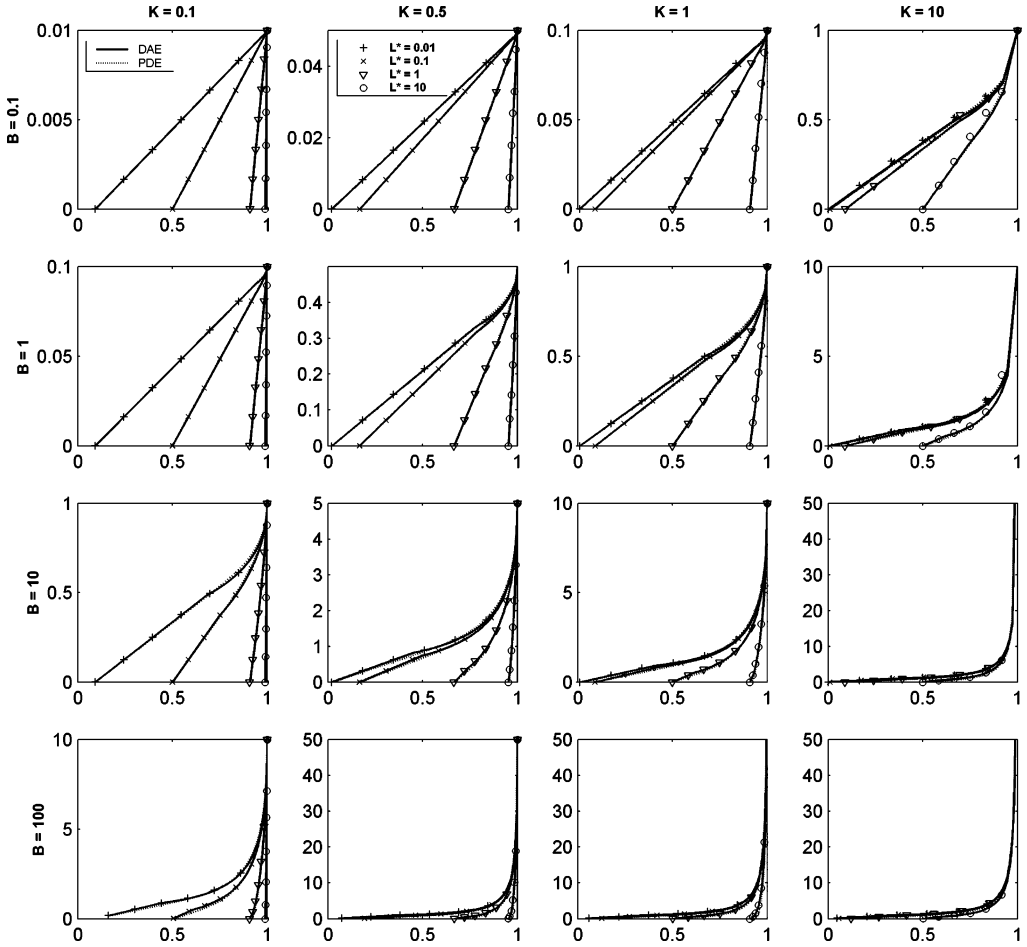

Figure 2. Dimensionless KPD $j^* = f(\bar{u})$ for a uniform initial concentration $u(x^*,\theta = 0) = 1$ and $u|_{x^*\to\infty}^{\theta=0} = 0$. Initial flux and final concentration values are, respectively, *BK* (the maximum of *y* scale is set to min (50, *BK*)) and ($L^*/K + L^*$). Solid lines are calculated from the DAE defined by eqs 12 and 16. Dotted lines are calculated from the numerical resolution of the corresponding PDE (eq 1 coupled with BC 4 and 7) via a quadratic finite element technique (see text for details).

The approach is illustrated in Figure 1. Since concerned IC and BC lead to regular solutions with weak curvature almost everywhere (i.e., high-order derivatives are very low), internal profiles are approximated by assuming $(\partial^m u/(\partial x^*)^m) = 0$, where m is an integer ≥ 3. $u(x^*)$ is, therefore, approximated by a parabolic profile. This approximation is realistic for fully developed profiles (i.e., local mass transport occurs for all range of x^*) but is incompatible for short time, because a sharp change in $(\partial^2 u/\partial x^{*2})$ propagates from the S−L interface toward the opposite side (or toward the geometric center of S if a symmetry plane is assumed). This last inconsistency is overcome by coupling the IC $u(x^*,\ \theta = 0) = \bar{u}|_{\theta=0} = 1$ with a parabolic profile at a moving theoretical interface (Figure 1 parts a and b). The position of the interface (noted x_i^*) defines two regions: a region with mass transport (for $x^* > x_i^*$) and a region without mass transport (for $x^* \leq x_i^*$). The so-defined coarse solution is by construction continuously differentiable at the interface, since it assumes a junction condition:

$$u|_{x_i^*} = \bar{u}|_{\theta=0} = 1 \quad \text{and} \quad \left.\frac{\partial u}{\partial x^*}\right|_{x_i^*} = 0 \quad \text{with} \quad 0 \leq x_{i^*} < 1 \tag{8}$$

Consequently, the dynamic regime with fully developed profiles is a prolongation of eq 12 for $x_i^* = 0$. Other ICs and BCs may be treated using similar approximations or by generalizing the concept of tracking interfaces where the Laplacian of u (i.e., $(\partial^2 u/\partial x^{*2})$) changes significantly.

2.2.1. Parabolic Solution for Fully Developed Profiles and Corresponding KPD Equation. The fully developed parabolic profile is uniquely defined by boundary constraints on its first derivatives, defined in eqs 2 and 7, at the S phase boundaries and by a particular value:

$$u(x^*) = \frac{1}{2}\left.\frac{\partial u}{\partial x^*}\right|_{x^*=1} x^{*2} + u|_{x^*=0} \tag{9}$$

From $j^* = (\partial u/\partial x^*)|_{x^*=1}$ and the definition of the residual concentration $\bar{u} = \int_0^1 u(x)\,\mathrm{d}x$, eq 9 becomes:

$$u(x^*) = \left(\frac{1}{6} - \frac{1}{2}x^{*2}\right)j^* + \bar{u} \tag{10}$$

The corresponding KPD equation $j^* = f(\bar{u})$ is inferred from eq 4 by replacing $u|_{x^*=1}$ by its value calculated via eq 10 and by defining the mass balance for the S phase from a change in $\bar{u}$ with time,

$$\int_0^\theta j^*(\tau)\,\mathrm{d}\tau = \bar{u}|_{\theta=0} - \bar{u} \tag{11}$$

which yields

$$j^*(\bar{u}) = -\frac{d\bar{u}}{d\theta} = B\cdot K\cdot\frac{\left(1+\frac{L^*}{K}\right)\cdot\bar{u} - \left(\frac{L^*}{K}\cdot\bar{u}\big|_{\theta=0} + u\big|_{x^*\to\infty}^{\theta=0}\right)}{1+\frac{1}{3}B\cdot K} = \underbrace{\alpha\cdot\bar{u}}_{j^*_D} - j^*_R \tag{12}$$

where $\alpha\,\bar{u} = j^*_{\mathrm{D}}$. From eq 12, the mass transfer between the S and L phases appears to obey a linear superposition of both first- and zero-order kinetics. The flux at the S−L interface is

consequently decomposed between a driving flux j^*_D proportional to $\bar{u}$ (proportionality coefficient α) and a resisting flux j^*_R independent of $\bar{u}$. As a result of $j^* = f(\bar{u})$ for constant B, K, and L^*, α is the slope of the characteristic curve and $-j^*_R$ is the intercept with $\bar{u} = 0$. The residual concentration at equilibrium is obtained from the intercept with $j^* = 0$ and is defined as the average state between ($\bar{u}|_{\theta=0}$, $j^* = 0$) and ($u|^{\theta=0}_{x^*\to\infty}$, $j^* = 0$), respectively, with the weights L^* and K:

$$\bar{u}|_{\theta\to\infty} = \frac{L^*\bar{u}|_{\theta=0} + Ku|^{\theta=0}_{x^*\to\infty}}{K + L^*} \tag{13}$$

All states ($\bar{u}$, j^*) are nonlinear functions of parameters B, K, and L^*. Table 1 summarizes typical values of α, j^*_R, and $\bar{u}|_{t\to\infty}$ for reduced cases of eq 11. The transport rate is maximal for $K \to \infty$ with $\alpha = 3$. The flux is then independent of B (i.e., hydrodynamic conditions) and of L^* (i.e., volume effect of the L phase). The condition $B \to \infty$ leads to a lower transfer rate so that the difference $j^*|_{K\to\infty} - j^*|_{B\to\infty}$ increases linearly with the amount of diffusant accumulated in the L phase $L^*/K(\bar{u}|_{\theta=0} - \bar{u})$. The condition $L^* \to 0$ (infinite dilution) yields a deviation $j^*|_{K\to\infty} - j^*|_{L^*\to 0}$, which is independent of $\bar{u}$ (without effect due to the diffusant accumulation in the liquid phase). This deviation also increases significantly when the product BK decreases as ($3BK/3 + BK$). From eq 6, diffusion within the S phase has no significant effect on the overall kinetic when the ratio (j^*/B) does not depend on B. This case corresponds to the denominator of eq 12 close to 1, that is, when $BK \ll 3$.

2.2.2. Coarse Solution for Short Time of Contact. According to Figure 1 and eq 8, the KPD equation for short time of contact is inferred from the last calculations (i) by replacing x in eq 9 by v with $v = (x^* - x_i^*)/(1 - x_i^*)$ (for $x_i^* \le x^* \le 1$) and $u|_{v=1} = \bar{u}|_{\theta=0}$, (ii) by noting $j^*(v) = (1/(1 - x_i^*))(\partial u/\partial v)|_{v=1}$, and (iii) by defining $\bar{u} = x_i^*\bar{u}|_{\theta=0} + (1 - x_i^*)\bar{u}^v$ with $\bar{u}^v$ being the averaged concentration between x_i^* and 1. This leads to eq 14:

$$u(v) = -\sqrt{\frac{3}{2}j^*(\bar{u}|_{\theta=0} - \bar{u})}v^2 + \bar{u}|_{\theta=0} \tag{14}$$

By replacing $u|_{x^*=1} = u|_{v=1}$ in eq 4 by its value given in eq 14, one gets

$$j^* + \underbrace{\left[B\cdot K\cdot\sqrt{\frac{3}{2}\left(\bar{u}|_{\theta=0} - \bar{u}\right)}\right]}_{b}\sqrt{j^*} - \underbrace{B\cdot\left[L^*\bar{u} + \left(K - L^*\right)\cdot\bar{u}|_{\theta=0} - K\cdot u|^{\theta=0}_{x^*\to\infty}\right]}_{c} = 0 \tag{15}$$

Equation 15 is a second-degree polynomial in $\sqrt{j^*}$, with a unique positive root, which yields

$$j^* = \frac{b}{2}[b - \sqrt{b^2 + 4c}] + c \tag{16}$$

To be physically consistent, eq 15 must verify the inequality $x_i^* = 1 - \sqrt{6(\bar{u}|_{\theta=0} - \bar{u}/j^*)} \ge 0$, that is $j^* \ge 6(\bar{u}|_{\theta=0} - \bar{u})$. In other cases, the hypothesis $u|_{v=1} = \bar{u}|_{\theta=0}$ is no longer valid and eq 16 must be used instead.

Equation 16 varies nonlinearly with $\bar{u}$ and parameters B, K, and L^*. By noticing that $b \to 0$ when $\bar{u} \to \bar{u}|_{\theta=0}$, a first-order approximation in $\bar{u}$ of the initial dynamic is inferred from a third-order expansion series in b of eq 16. It yields

$$j^* = c - \sqrt{c}b + \frac{b^2}{2} + o(b^3) \tag{17}$$

The approximation (eq 17) demonstrates that j^* is decreasing and convex with an initial value $j^*|_{\theta=0} = BK(\bar{u}|_{\theta=0} - u|^{\theta=0}_{x^*\to\infty})$. The very initial decrease in j^* when $\bar{u}$ decreases is controlled by the first term c, which is very similar to eq 12. For larger decreases in $\bar{u}$ and large values of the product BK, j^* exhibits a significant curvature, which is responsible for the discrepancy in the KPD shape between short-time contact (STC) and fully developed parabolic (FDP) regimes. Higher-order expansions of eq 16 demonstrate that the curvature of $j^* = f(\bar{u})$ decreases when $\bar{u}$ decreases down to a minimal value when b is close to $(4/3)\sqrt{c}$. j^* is then converging to a straight line defined by

$$j^* = \frac{BK}{1 + \frac{3}{2}BK}\left[\frac{L^*}{K}\bar{u} + \left(1 - \frac{L^*}{K}\right)\bar{u}|_{\theta=0} - u|^{\theta=0}_{x^*\to\infty}\right] \tag{18}$$

At their intersection, eqs 12 and 18 provide only an approximation of class C^0 of KPD. A continuous approximation of class C^1 is, however, achieved for small values of BK, since eqs 12 and 18 have close slopes at their intersection.

2.3. Typical Kinetic Phase Diagrams. 2.3.1. Comparisons between KPD Approximations from Algebraic Differential Equation (DAE) and Finite Element (FE) Techniques. The DAE $-$ ($d\bar{u}/d\theta$) $= j^*(\theta, \bar{u})$ defined by eqs 12 and 16 was efficiently solved for $\bar{u}|_{\theta=0} = 1$ via a quasi-constant step-size implementation of the numerical differential formulas (NDF) in terms of backward differences.[17] The results obtained from the DAE formulation and with a direct but more time-consuming numerical resolution of the PDE problem are compared in Figure 2. The PDE defined by eqs 1, 4, and 7 was solved using a finite element technique (FE) based on 50 uniformly distributed nodes and quadratic elements. A same-time marching procedure based on variable-order NDF formula (order between 2 and 5) was used for both DAE and FE formulations. In the FE formulation, the flux j^* was calculated analytically from eq 8 on the basis of the available estimations of $\bar{u}$ and $u|_{x^*=1}$.

Approximations of $j^* = f(\bar{u})$ from DAE and FE formulations yield similar results during STC and FDP regimes and, thus, confirmed consistency of the proposed approximation. The total computational time with the DAE was, however, reduced by a factor between 100 and 1000 for the same code implemented in Fortran 90.

2.3.2. Typology of KPD Shapes. In Figure 2, extreme shapes of KPD correspond to a straight line and a hyperboliclike shape for $BK \ll 1$ and $BK \gg 1$, respectively. Cases with intermediate BK values are identified by an intermediate convexity during the STC regime. For $L^* \ll 1$, intermediate cases are not discernible. Intermediate KPD obtained for $L^* = 0.01$ and the same $BK = 1$ (respectively, 0.1×10, 1×1, and 10×0.1) thus yields similar results. For higher values of L^*, intermediate cases are discernible from the change in either KPD slope during FDP regime or equilibrium state.

2.3.3. Estimation of the Equilibrium State Based on KPD. Figure 2 confirms that the final state may be easily linearly extrapolated from the FDP regime. As a result, the equilibrium state becomes observable (i.e., predictable) as soon as the intercept of the KPD tangent with $j^* = 0$ is close enough to the equilibrium value ($L^*/K + L^*$). By means of the reduced concentration, $X = (\bar{u}|_{\theta=0} - \bar{u}/\bar{u}|_{\theta=0} - \bar{u}|_{\theta\to\infty})$, an exponential law was fitted to estimate which minimal fraction X_{min} of the whole KPD diagram was derived to predict the equilibrium state for a particular value of the product BK:

$$X_{min} = 85\%(1 - e^{0.134BK}) \tag{19}$$

Equation 19 illustrates that ~10% of the whole kinetic must be observed to estimate accurately the equilibrium state if $BK = 1$, whereas more than 70% and 85% must be observed for, respectively, $BK = 10$ and $BK \gg 1$.

The previous strategy may be extended to variable external conditions with time (dilution effect, variation in stirring, and change of solvent) by vertically translating the current last "observed" state from $(\bar{u}, j_1^*|_{\bar{u}})$ to $(\bar{u}, j_2^*|_{\bar{u}})$, where numbers 1 and 2 are related to the KPDs corresponding to the old and new conditions, respectively. The new "possible" equilibrium is, therefore, approximated from the linear prolongation of the new state with the previous slope (only j_R^* is updated) or, more accurately, with the new slope when it is available or known (both α and j_R^* are updated).

2.4. Comments on the Feasibility of the Simultaneous Estimation of *D*, h_m, and *K* from KPD Abacus and Experimental Data. KPD shapes suggested that the transport properties (D and h_m) and the partition coefficient (K) cannot be estimated at the same time with the same accuracy from an experimental data set $(\bar{u}, j^S = (D/l_S)j^*)$, where j^S is a scaled flux in $m \cdot s^{-1}$ (flux related to an initial concentration of 1). This subsection examines theoretically how the extraction of different information from STC and FDP can improve the well-poseness of the identification of the three properties.

2.4.1. Strategy Based on the Combination of Information Available during STC and FDP Regimes. A rough estimation of the dependence between parameters is provided from the analytical expression of the most typical and independent characteristics of the scaled KPD for both the STC and FDP regimes. For the three unknown parameters, we choose three characteristics: the initial state $(1, j^S|_{\theta=0})$, an estimate of the KPD curvature $\beta_{\bar{u}|_{STC}}(b^2|_{\bar{u}|_{STC}}{}^S/2)$ for a particular state during the STC regime $(\bar{u}|_{STC}, j|_{STC})$, and finally the equilibrium state $(\bar{u}|_{\theta\to\infty}, 0)$. These characteristics estimated from eqs 17 and 12 lead to the following system:

$$\begin{cases} j^S|_{\theta=0} = \dfrac{DBK}{l_S} = hK \\ b^2|^S_{\bar{u}|_{STC}} = \beta_{\bar{u}|_{STC}} \dfrac{DB^2K^2}{l_S} \propto l_S \dfrac{(hK)^2}{D} \\ \bar{u}|_{\theta\to\infty} = \dfrac{L^*}{K + L^*} \end{cases} \tag{20}$$

It follows that the unique solution is

$$\begin{cases} D \propto l_S \dfrac{(j|_{\theta=0})^2}{b^2|^S_{\bar{u}|_{STC}}} \\ h \propto \dfrac{1}{L^*} j^S|_{\theta=0} \dfrac{1 - \bar{u}|_{\theta\to\infty}}{\bar{u}|_{\theta\to\infty}} \\ K \propto L^* \dfrac{1 - \bar{u}|_{\theta\to\infty}}{\bar{u}|_{\theta\to\infty}} \end{cases} \tag{21}$$

where, in the case of incomplete data (nonobserved equilibrium), $\bar{u}|_{\theta\to\infty}$ may be estimated from the α value (eq 12) and a particular state during the FDP regime $(\bar{u}|_{FDP}, j^*|_{FDP})$:

$$\bar{u}|_{\theta\to\infty} = \frac{L^* j^*|_{FDP}[3\beta_{\bar{u}|_{STC}} j^S|_{\theta=0} + b^2|^S_{\bar{u}|_{STC}}] - 3b^2|^S_{\bar{u}|_{STC}} \bar{u}|_{FDP}}{L^* j^*|_{FDP}[3\beta_{\bar{u}|_{STC}} j^S|_{\theta=0} + b^2|^S_{\bar{u}|_{STC}}] - 3b^2|^S_{\bar{u}|_{STC}}} \tag{22}$$

Consequently, an estimation of the initial flux (or that during the STC regime) is required for both transport properties, h_m and D. Besides, the observation of the kinetic must be long enough and with appropriate sampling to make possible the estimation of the KPD curvature with enough accuracy. In the presence of large unscaled time data, a poor estimation may lead to unreliable transport properties. The relative error in D is proportional to the product of relative errors in $j^S|_{\theta=0}$ and $b|^-{}_{u|_{STC}}$, whereas the relative errors in h_m and K vary like $1/(\bar{u}|_{\theta\to\infty})^3$. Thus, for a coupled estimation of the three parameters, the quality of the estimation of D depends mainly on the dynamics during STC regime, whereas both h_m and K are very sensitive to the quality of the prediction of the equilibrium state derived from data available during the FDP regime.

An accurate estimation of the dimensionless B number requires information from both the STC and FDP regimes:

$$B \propto \frac{1}{L^*} \frac{b^2|^S_{\bar{u}|_{STC}}}{j^S|_{\theta=0}} \cdot \frac{1 - \bar{u}|_{\theta\to\infty}}{\bar{u}|_{\theta\to\infty}} \tag{23}$$

2.4.2. Strategies Based Only on the Information Available during the FDP Regime. Identification strategies based only on the FDP regime do not provide enough information to estimate all three parameters. This impossibility is confirmed by KPDs that are completely determined by two parameters or particular states (see eq 12). Nevertheless, this difficulty may be overcome if different achievements of scaled $\alpha^S = 3(K + L^*)(3hD/3D + hl_SK)$ are available for different values of L^* and/or l_S. Different slopes as well as different equilibrium states are then achieved and make possible the theoretical calculation of the three properties.

3. Materials and Methods

3.1. Desorption Experiments. In unsteady mass transfer conditions, the experimental determination of KPD $(j = f(C_L))$ is difficult since j cannot be measured directly and independently. It is conventionally derived from the differentiation of C_L with time (see Section 3.1.3). The accuracy of j estimates depends strongly on the sampling rate and on the noise level in C_L measurements.

Desorption kinetics with relative high frequency were achieved by monitoring the concentration rise of a UV tracer, 2,5′-dimethoxyacetophenone (DMA), within a stirred suspension of LDPE (low-density polyethylene) particles. DMA is a relatively fast-diffusing substance, with a maximum absorbance at 330 nm, and is sparingly soluble in polar solvents (log $P \approx 2.1$).

3.1.1. Solid-Phase Preparation. LPDE resin containing DMA at 0.6% (w/w) was prepared by initiallly soaking virgin LDPE powder (particle size 300 μm) into a methanol solution with DMA and by subsequently vaporizing the solvent under vacuum. Dyed powder was extruded the same day, than soaked in a four-temperature-zone monoscrew extruder (model Scamia RHED 20.11.D, France; set zone temperatures: 125, 130, 135, and 135 °C) and laminated to yield a 30 mm × 0.5 mm ribbon. Died ribbon was stored at −18 °C before use. The ribbon was finally transversally cut with a microtome so as to provide particles with the following sizes: $2l_S \times l_1 = 0.5$ mm and $2l_S \times l_2 = 20 \pm 5$ mm, where $2l_S$ ranged between 3 and 100 μm. The uniformity of cut and tracer concentration was controlled from microscopic observations (UV charge-coupled device (CCD) camera, model Hamatsu-C4742-95812E5, coupled with a UV microscope, model Karl Zeiss -MPM800MCS) at constant transmitting light wavelengths, respectively, 420 and 330 nm.

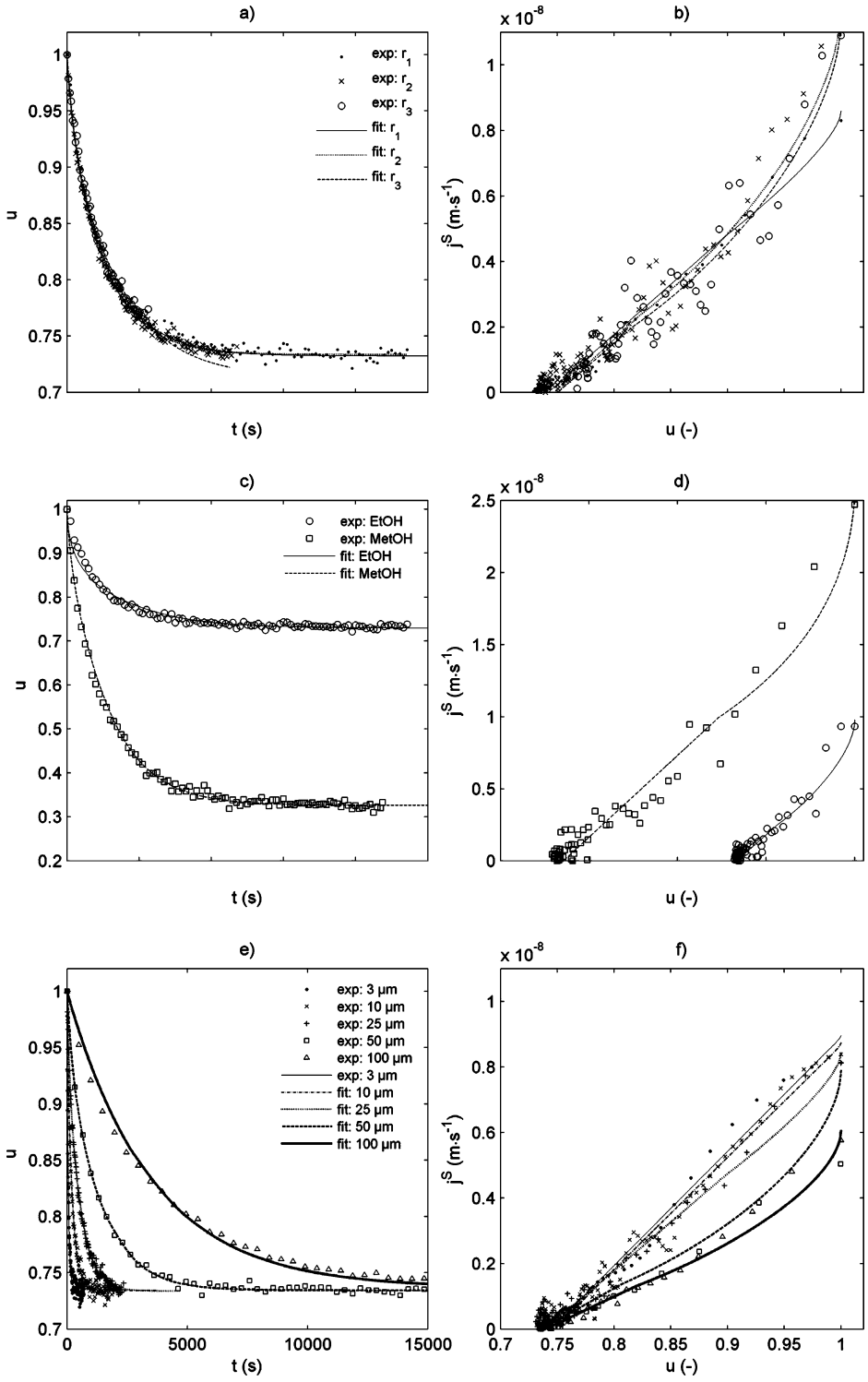

Figure 3. (a,c,e) Experimental desorption kinetics, (b,d,f) corresponding KPD $j^S = f(\bar{u})$. The conditions were as follows: (a,b) reference conditions ($2l_S$ = 50 μm particles in ethanol, $L^* = 7.2 \times 10^{-3}$) with three repetitions noted $\{r_i\}_{i=1...3}$; (c,d) $2l_S = 50$ μm in ethanol (noted EtOH) and methanol (noted MetOH), respectively; (e,f) $2l_S = \{3,10,25,50,100\}$ μm in ethanol. Experimental and fitted data are plotted with symbols and lines, respectively.

Experiments were set up with thin particles to ensure (i) one-dimensional mass transfer (i.e., side effects were assumed to be negligible since $l_1/l_S \geq 10$) and (ii) low B values that ranged between 1 and 10^3. The latter conditions ensured that both diffusion and external resistances were acting simultaneously on desorption.

3.1.2. Liquid-Phase Preparation. Ethanol and methanol (99% purity) were chosen as L phase to make possible the sedimentation of particles and to provide different K values.

3.1.3. Desorption Cell and On-line C_L Measurement. The desorption step was performed at 20 °C in quartz 3 mL cells located inside a thermostatic modified spectrophotometer (model Shimadzu−UV2401 PC), including a miniaturized immersed magnetic stirrer (stirring velocity 200 rpm). The cell position was adjusted so that the beam crossed the suspension at ∼10 mm from the cell bottom and below a possible vortex at the air−liquid interface. The reference was set up from an identical cell filled with the liquid-phase alone but not stirred.

Absorption intensities were continuously acquired with an acquisition rate up to 20 Hz. The spectrum was scanned between 280 and 480 nm with an acquisition period varying between 10 and 40 s. After numerical treatment, only the maximal intensity of each spectrum (at 330 nm) was used to assess the concentration in DMA. The numerical treatment consisted of digital filtering (noncausal digital filter with cutting-off frequency of 0.5 Hz with 60 db attenuation) and of subsequently subtracting the baseline generated by turbidity (estimated between 400 and 460 nm). It was verified with nondyed LDPE particles in suspension in reference DMA solutions that either maximum values at 330 nm or cumulative values between 280 and 400 nm of corrected spectra provided similar results and were linearly correlated to reference DMA concentration values. In addition, it was established that the calibration curve was not sensitive to the stirring velocity in the range 0−400 rpm. It is worth noticing that our procedure measured only the DMA absorbance in the solution and not that within the solid particles.

3.2. Numerical Procedure for the Assessment of KPD Features (j^S, $dj^S/d\bar{u}$) from C_L Measurements. 3.2.1. Macroscopic Mass Balance in Diffusing Substance. Experimental KPD were expressed as $j^S = f(\bar{u})$ and were calculated by assuming no DMA loss between solid and liquid phases:

$$\begin{cases} \bar{u}(t) = 1 - \dfrac{1}{L^*}\cdot\dfrac{C_L(t)}{C_P(t=0)} \\ j^S(t) = \dfrac{1}{C_P(t=0)}\cdot\dfrac{1}{l_L}\dfrac{dC_L(t)}{dt} \\ \dfrac{dj^S}{d\bar{u}}\Big|_{(t)} = -\dfrac{1}{C_P(t=0)}\cdot\dfrac{L^*}{l_L^{\,2}}\cdot\dfrac{1}{j^S(t)}\dfrac{d^2C_L(t)}{dt^2} \end{cases} \quad (24)$$

3.2.2. Continuous Estimations of First and Second Time Derivatives of C_L. The direct application of eq 24 requires one to approximate first and second derivatives (dC_L/dt) and (d^2C_L/dt^2) with sufficient accuracy when C_L is subjected to noise and includes possible changes in acquisition rate. To not spread experimental errors between the STC and FDP regimes, nondeterministic local and differentiable approximates of $C_L(t)$ were preferred to a global continuous fitting function. Such methodologies provide an extension to classical regression techniques by combining both filtering techniques (weighting kernels) and maximum likelihood strategies via the introduction of constraints such as smoothness or a priori knowledge.[18,19] For a data set $\{t_i, C_L|_{t_i}\}_{i=1...M}$ including M samples, each $\{C_L|_{t_i}\}_{i=1...M}$ and its derivatives are locally approximated from a local polynomial regressor of degree k, noted $\{\tilde{\psi}_{l,i}\}_{l=0...k,i=1...M}$. For each sampling time t_i, polynomial coefficients $\psi_{\bullet,i}$ are defined in the local normalized base, 1, $\tilde{t}_i$, ..., $\tilde{t}_{\tilde{t}i}^{\,k}$, where ($\tilde{t}_i = (t - t_i)/\tau$). τ is a positive constant defined in eq 26. The whole approximation problem is assembled as M Tikhonov regularized least-squares problems[20] and solved using M singular-value decompositions as described by Hansen:[21]

$$\tilde{\psi}_{\bullet,i} = \min_{\psi_{\bullet,i}} \sum_{j=1}^{M} \{[\omega_{ij}\cdot(C_L|_{t_i} - \sum_{l=0}^{k} K_{jl,i}\cdot\psi_{l,i})]^2 + \xi^2\cdot(\sum_{l=0}^{k} D_{jl,i}{}^{m}\cdot\psi_{l,i})^2\} \quad \text{for all } i = 1...M \quad (25)$$

where $\{K_{jl,i}\}_{1\le j\le M,0\le l\le k,1\le i\le M}$ are the local Vandermonde matrices defined by $\tilde{t}_{\tilde{t}j}^{\,l}$, $\{D_{jl,i}{}^{m}\}_{M,0\le l\le k,1\le i\le M}$ are the corresponding mth-order differentiation matrices, $(l!/(l-m)!)\tilde{t}_i^{\,l-m}$, and ξ^2 is a positive scalar that controls the tradeoff between the closeness to the data and the smoothness. ω_{ij} is a symmetric (i.e., noncausal) weighting kernel used for low bypass filtering data points by decreasing their influence in each local interpolation sequence according to their distance from t_i. Moving overlapping windowing was applied using a tricube kernel with support on $[-1, 1]$,

$$\omega_{ij} = \left[\max\left(1 - \left|\frac{t_j - t_i}{\tau}\right|^3, 0\right)\right]^3 \quad (26)$$

where τ is the so-called bandwidth, which restricts only the observations in the interval $[t_i - \tau, t_i + \tau]$ to be used for the identification of $\psi_{\bullet,i}$. As a result, $\{\tilde{\psi}_{\bullet,i}\}_{i=1...M}$ are envisioned as the best local polynomial approximates of degree k with the smallest mth derivative at time t_i (i.e., almost equivalent to a smoothing spline of order $2m$ with a break at every data site).

Because of the high regularity of the true solution C_L, the best results were obtained by choosing $k = 4$, $m = 3$, and $\tau = 1500$ s and by assuming symmetric boundary conditions at both ends of the measured signal. Finally, $j^S|_{t_i}$ and $d_j^S/d\bar{u}|_{t_i}$ were analytically calculated from $\{\tilde{\psi}_{\bullet,i}\}_{i=1...M}$ derivatives at time t_i using eq 24. For the same trial, the uncertainty at time t_i in each local regressor value and its derivatives were estimated from standard deviations related to $C_L|_{t_i}$ and $j^S|_{t_i}$, noted, respectively, $\sigma_{(t_i)}^{C_L}$ and $\sigma_{(t_i)}^{j}$, and derived from the diagonal elements of the covariance matrix of the local regularized least-squares problem defined by eq 28. Each covariance matrix was calculated by means of an orthogonal-triangular decomposition (QR) of the local regression operator A_i defined by eq 27 and a singular-value decomposition of the so-computed matrix R_i.

$$A_i = \begin{bmatrix} W_{\bullet\bullet,i}K_{\bullet\bullet,i} \\ \zeta D_{\bullet\bullet,i} \end{bmatrix} = Q_iR_i \quad (27)$$

where $W_{jj,i} = \omega_{ij}$ and $W_{jl,i} = 0$ for $j \neq l$.

A similar procedure was used to assess the standard deviation related to $(dj/dC_L)|_{t_i}$, noted $\sigma_{(t_i)}^{dj/dC_L}$, from a local approximation of the KPD $\{C_L|_{t_i}, \hat{j}|_{t_i}\}$ based on a bivariate weighting kernel, which takes into account errors on both variables. The regularization parameter ξ^2 was chosen to globally minimize the confidence intervals on first derivatives.

3.3. Generalized Least-Squares Criterion to Identify $p = [D, K, h_m]'$. Transport properties were simultaneously identified by minimizing a generalized least-squares criterion incorporating the main features of KPD,

$$\chi^2(p,d,M) = d\sum_{i=1}^{M}\left\{\lambda_1\left[\frac{C_L|_i - \hat{C}_L(t_i,p)}{\sigma_{C_L}|_i}\right]^2 + \lambda_2\left[\frac{j^S|_i - \hat{j}^S(t_i,p)}{\sigma_j^S|_i}\right]^2 + \lambda_3\left[\frac{\dfrac{dj^S}{d\bar{u}}\Big|_i - \dfrac{d\hat{j}^S(t_i,p)}{d\hat{u}}}{\sigma_{dj^S/d\bar{u}}|_i}\right]^2\right\} + P(p,d) \quad (28)$$

where $d = 1, 2, 3$ is the dimension of the kinetic approximation space and $\{\lambda_i\}_{i=1...d}$ are coefficients that verify $\sum_{i=1}^{d}\lambda_i = 1$ and balance the deviations in magnitude of the distance function according to the source of information available at time $\{t_i\}_{i=1...M}$. $\hat{X}$ and σ_X denote predicted values of X from the

Table 2. Estimated Values of Parameters *D*, *K*, *h*, and *B* (Row *a* = 2.5th Percentile, Row b = Median Value, Row *c* = 97.5th Percentile) According to Both Identification Procedures: *d* = 1 or *d* = 2

parameter		$D \times 10^{13}$ ($m^2 \cdot s^{-1}$)		$K \times 10^3$		$h \times 10^6$ ($m \cdot s^{-1}$)		*Bi*	
criterion		*d* = 1	*d* = 2	*d* = 1	*d* = 2	*d* = 1	*d* = 2	*d* = 1	*d* = 2
r_1	a	0.16	1.3	2.6	2.5	5.4	3.3	290	110
	b	0.41	1.8	2.6	2.6	6.3	3.5	1.9×10^3	240
	c	2.3	3.9	2.7	2.6	93	4.3	7.3×10^4	410
r_2	a	0.17	1.1	2.6	2.4	4.9	4.3	430	256
	b	0.29	1.5	2.6	2.4	5.6	4.8	2.4×10^3	650
	c	1.4	2.1	2.7	2.5	74	5.3	5.4×10^4	770
r_3	a	0.33	0.84	2.1	2.2	5.8	4.7	300	450
	b	0.48	0.96	3.1	2.4	6.2	5	2.3×10^3	630
	c	2.4	1.3	3.9	2.6	78	5.2	5.4×10^4	950
EtOH′	a	0.14	1.1	2.6	2.4	4.4	3.4	240	160
	b	0.18	1.6	2.7	2.6	11	3.8	7.6×10^3	300
	c	2.3	2.7	2.7	2.8	170	4.2	1.5×10^5	480
MetOH	a	0.77	1.8	15	12	2.8	1.4	290	46
	b	0.9	2.4	15	14	3.8	1.6	530	83
	c	1.2	3.8	15	16	56	1.9	9.1×10^3	130
3 μm	a	0.043	4.1	2.6	2.2	3.8	2.8	100	5
	b	0.069	5.7	2.6	2.4	5.1	3	1.1×10^2	8
	c	0.55	7.8	2.6	2.7	66	3.2	2.3×10^4	12
10 μm′	a	0.16	2.6	2.6	2.4	4.6	1.9	100	7
	b	0.2	6.1	2.6	2.6	6.4	2	1.6×10^3	16
	c	2.4	14	2.6	2.9	63	2.6	1.9×10^4	50
25 μm	a	0.63	0.79	2.6	2.4	4	3.1	82	140
	b	0.7	15	2.6	2.5	5.4	3.3	964	280
	c	6.1	2.7	2.6	2.6	61	3.5	1.2×10^4	550
50 μm	a	1.7	0.63	2.6	2.3	3.9	3	305	210
	b	2.4	1.5	2.6	2.4	4.2	3.9	438	650
	c	3.2	3.6	2.6	2.5	46	5.0	6.8×10^4	2.0×10^3
100 μm	a	0.82	1.7	2.6	2.5	3.2	2	84	420
	b	1.02	3	2.6	2.6	3.3	3.4	1.7×10^3	850
	c	19	2.4	2.6	2.6	35	5.3	2.1×10^4	1.6×10^3

physical model (see Section 2.1) and estimates of error in X, respectively. $P(p,d)$ is a smooth and continuous penalty function based on Heaviside distributions, which gives a large value when physical infeasibility is encountered and gives 0 elsewhere. Classical identification is reduced to the particular case $d = 1$ and $\lambda_2 = \lambda_3 = 0$.

Because of the high nonlinearity of the distance function and efficiency, eq 28 was minimized using a downhill simplex method that did not use the gradient information of $\chi^2(p,d,M)$. After an initial raw exploration, optimization proceeded by successive contractions toward a minimum $\hat{p}$ that may be a local minimum and possibly different of the true one if $\chi^2(p,d,M)$ is biased.

The property of $\hat{p}$ to be a global minimum of eq 28 was tested by mapping the values of on a $\chi^2(p,d,M)$ $20 \times 20 \times 20$ mesh contracted around the identified $\hat{p}$ value. Since errors in parameter values of several magnitude orders might be expected, a logarithmic scale was used. A contour of constant $\Delta\chi^2$ was used as the boundary of the identification confidence region. As prescribed by Press et al.,[22] a Monte Carlo sampling was finally applied to determine which contours corresponded to 80%, 90%, and 95% joint confidence regions. The determinant of the formal Fisher information matrix $F = J'J$ at the minimum $\hat{p}$ was used as a qualitative interpretation of the variance of $\hat{p}$, where J was the Jacobian of the model.

4. Experimental Section

Raw spectra of suspensions presented disrupted and biased signals including up to 40% of noise. Filtering and bias correction removed outliers and reduced errors below 10%. The absorption at the wavelength of 330 nm was used to estimate C_L and subsequently $\bar{u}$. Experimental kinetics, $\bar{u}_{(t)}$, and KPD, $j^S = f(\bar{u})$, are synthesized in Figure 3. Identified values and 95% confidence intervals of D, K, h, and B, identified from data plotted in Figure 3 are summarized in Table 2. It is emphasized that j^S is expressed in $m \cdot s^{-1}$ and is equivalent to the reciprocal of an overall mass transfer resistance between the solid and liquid phases.

4.1. Typical Kinetics and KPD for Reference Conditions. Parts a and b of Figure 3 present results obtained for reference desorption conditions ($2l_S = 50$ μm, in ethanol, $L^* = 7.2 \times 10^{-3}$). Desorption kinetics were acquired in triplicates (repetitions are noted $\{r_i\}_{i=1..3}$) until equilibrium for repetitions r_1 and r_2 and for a desorption level of 90% for repetition r_3. The fluctuations of $\bar{u}_{(t)}$ at equilibrium showed a random noise level up to 10% of the observed variation scale. Errors between repetitions had the same order of magnitude and confirmed the good repeatability of both the sampling procedure and the acquisition one. The three experimental kinetics were, therefore, similarly fitted with a $d = 1$ model (Figure 3a). The main difference was observed for the r_3 kinetic that led to different asymptote.

Experimental and fitted KPD ($d = 2$ criterion) also exhibited good repeatability. 95% confidence intervals assessed for all repetitions and extracted from the covariance matrix of local regressors were similar and about 5% and 15% of the full variation scale for $\bar{u}$ and j^S, respectively. Fitted KPD decreased monotonically with a low curvature, whereas experimental KPD evolved as wavy decaying trajectory with an increasing frequency when $\bar{u}$ was decreasing. The deformation of the time-frequency domain in KPD space was responsible of such an apparent acceleration of oscillations.

For the same starting guess and identification strategy, all repetitions yielded similar values for D, K, h_m, and B (Table 2). Large differences in D and B values up to 2 decades were, however, observed between $d = 1$ and $d = 2$ criteria. Criteria based on $d = 3$ gave similar results and are not shown. The sensitivity analysis confirmed that the confidence intervals were

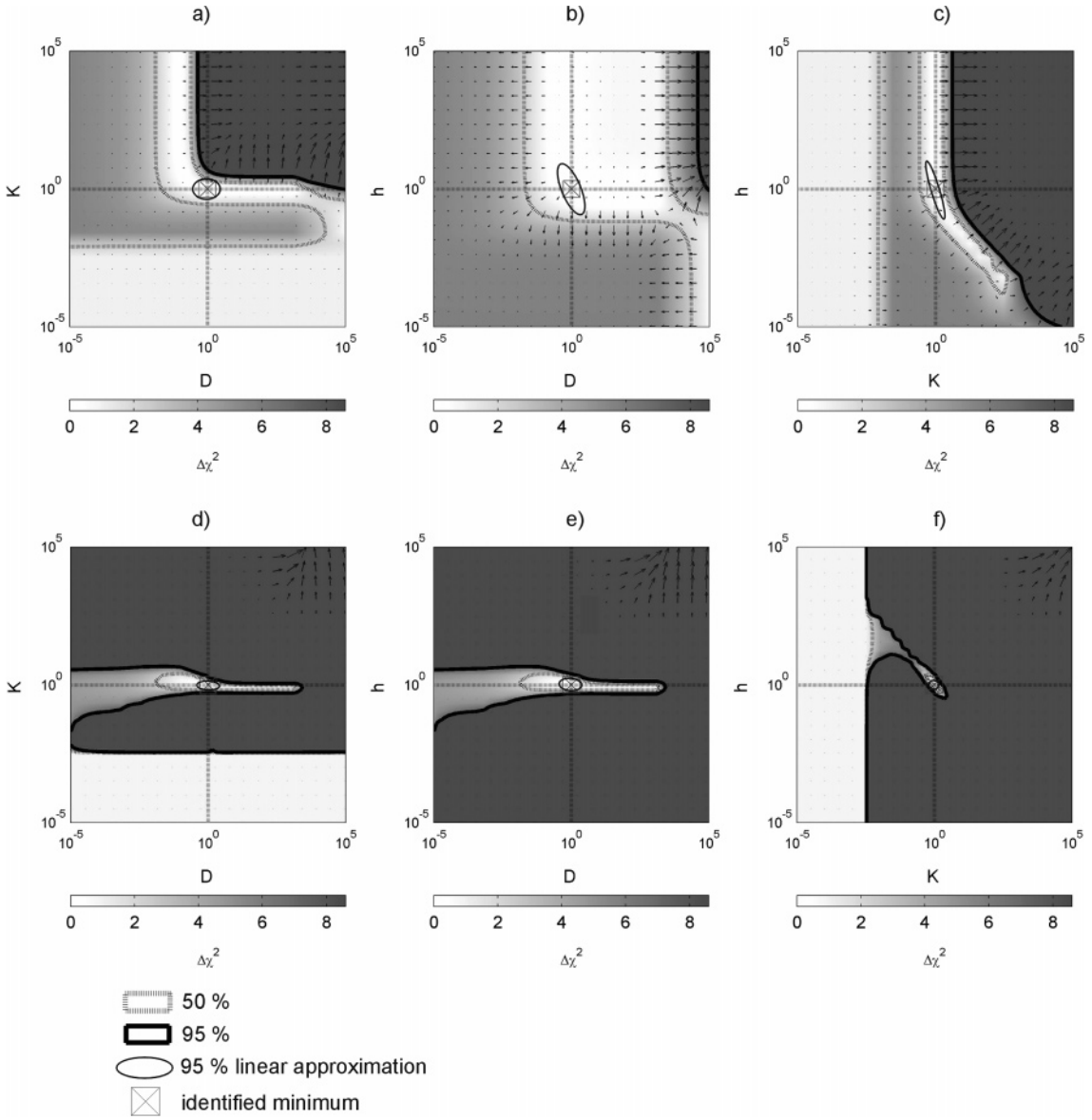

Figure 4. Projected joint confidence regions (PJCR) derived from results depicted in Figure 3 parts a and b (repetition r_3). PJCR were based on criteria calculated for (a,b,c) $d = 1$ and (d,e,f) $d = 2$. Gray level values represent $\min(\Delta\chi^2,8)$. The gradient of $\Delta\chi^2$ is superimposed as quiver plots. PJCR based on an approximation of the local information matrix is also indicated. The axes of projections are plotted in dotted lines and correspond to identified values of D, K, and h_m. The deviation between the identified minimum and the intersection of the projection axis assesses the bias due to the identification procedure.

greater for $d = 1$ (significantly above 1 decade) than for $d = 2$ (less than a factor 3). In addition, it was verified that estimated values with $d = 1$ were not centered within the confidence interval and corresponded mainly to local minimums. These results confirmed experimentally that both transport properties D and h_m cannot be inferred independently from raw kinetic data. The accuracy was besides dramatically increased with an approximation space taken into the mass flux ($d \geq 2$).

As expected, similar K values were derived with high confidence for all tested d values when the equilibrium state was observed during the experiment (repetitions r_1 and r_2). When it was not observed, $d = 1$ criterion gave only local minimums ranged with a confidence interval up to a factor 2 (repetition r_3). Additionally, removing the last points of the kinetic r_3 (such that $u > 0.7$) increased the previous uncertainty by a factor 2. This effect was not observed for $d \geq 2$ criteria.

4.2. *K* Effect. Parts c and d of Figure 3 present the desorption kinetic and KPD when ethanol is replaced by methanol as L phase for reference desorption conditions (for $0.4 < L^*/K < 4$ according to Table 1). The desorption rate in methanol was much higher than that in ethanol. Kinetics and KPD exhibited similar shapes, respectively. KPDs were, in particular, almost homothetic when a FDP regime, identified by a linear section, was achieved in the material. According to eq 12, this condition corresponded to $BK \ll 3$, which entails that the KPD slope was mainly controlled by the value of h_m in both L phases.

The criterion $d = 1$ failed to identify a similar D value for both conditions (Table 2). By contrast, the homothetic curvature in KPD shape during STC made it possible to determine a very similar D value. The existence of an STC regime was verified by noticing that the linear extrapolation of the FDP regime led to a different initial state (for $\bar{u}|_{t\to 0}$) with a lower desorption rate $j^S|_{t\to 0}$. Besides, the final equilibrium state was completely determined starting from the transition state between the FDP and STC regimes (before 40% of the whole migration occurred).

4.3. l_S Effect. Parts e and f of Figure 3 plot the effect of thickness for $2l_S$ varying from 3 to 100 μm in reference desorption conditions. As expected, desorption kinetics were drastically modified when the thickness was changed. By comparison, the modifications in KPD were less noticeable. For

$2l_S < 25\ \mu$m, KPD were linear in shape with the same maximum normalized flux ($j^S|_{t\to 0}$) of $\sim$0.9 m•s^{-1}. For $2l_S > 25\ \mu$m, KPD exhibited a significant curvature and showed a maximum normalized flux ($j^S|_{t\to 0}$) that decreased when l_S increased. These simple observations are interpreted as the external mass transfer resistance controls, mainly the desorption kinetic, for low thicknesses, whereas a combination of both internal and external resistances act on desorption when the thickness is higher. The increase in the value of B when the thickness increased confirmed this interpretation of KPD.

Transport properties based on $d = 1$ were poorly identified; their quality depended strongly on the thickness, on the true B value in fact. However, the errors between both properties D and h_m were highly correlated during the identification so that any reliable determination of the true B was not possible (Table 2).

By contrast, D, h_m, and B results based on $d = 2$ were more robustly identified. The uncertainty and bias in h_m and D were reliably distinguished. Thus, a $d \geq 2$ methodology yielded low overestimated D values for low thicknesses, whereas the $d = 1$ methodology underestimated systematically the true D value by a factor up to 20 in similar conditions.

4.4. Typical Projected Confidence Regions. Typical projected confidence regions (PJCR) are compared in Figure 4 for both $d = 1$ and $d = 2$ methods applied to the data set r_3 (Figure 4 parts a and b). Both methods led to highly different topologies, an extruded "L" shape oriented along the h_m dimension and an "I" shape oriented along the D dimension for $d = 1$ and $d = 2$, respectively.

For $d = 1$, the orientation of the confidence ellipsoid confirms that errors in estimated D and h_m were strongly correlated (Figure 4b). Furthermore, the low convexity of the criterion at its minimum showed that the upper limits of D and h_m were poorly bounded. This behavior explained why individual confidence intervals of both transport properties where noncentered on the found minimum value.

Such drawbacks were not observed with a $d \geq 2$ criterion (Figures 4 parts d, e, and f). $d = 2$ yielded PJCR with deep valleys with almost isotropic properties at the minimum. The number of feasible situations was drastically decreased. The increase in well-poseness (optimality) of the least-squares problem was estimated by the trace and determinant of the information matrix. The variance of parameters was respectively decreased six times (A-optimality property), and the volume of the confidence ellipsoid of the regression estimates was decreased by a factor 5×10^3 (D-optimality property).

5. Numerical Experiments

The effects of desorption level defined by $s = [1 - \min_\theta(\bar{u}|_\theta)]/(1 - \bar{u}|_{\theta\to\infty})$ and of K, L^*, and B values on both bias and confidence on D, h_m, K parameters in controlled conditions of noise and sampling were assessed more systematically by numerical experiments. The maximum ratio l_S^2/D was set to 4 $\times$ 10^5 s (4.6 days) to enclose the conditions experimentally explored. Kinetics were based on 20 simulated concentration data points that were sampled (i) at constant frequency (uniform sampling in time) or (ii) so that the variation in concentration between consecutive data points was constant (uniform sampling in concentration). Both situations corresponded to two extreme cases for the repartition of data in KPD. All data were blurred with 5% white noise and truncated according to min(1, u). Dimensionless KPD, $j^* = f(\bar{u})$, were reconstructed as previously from eqs 24 and 25.

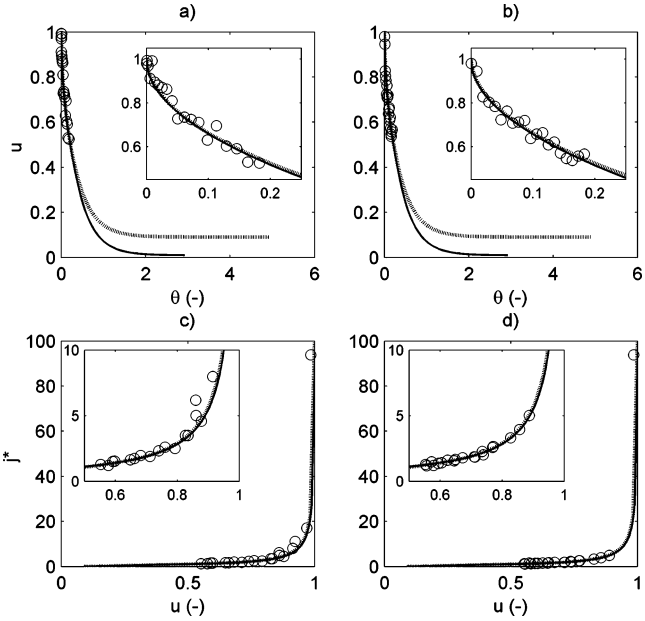

Figure 5. Simulated dimensionless desorption kinetics ($B = 1000$, $K = 0.1$, $L^* = 0.01$, and $s = 50\%$): (a,b) raw kinetics and (c,d) corresponding KPD. Simulated data were based on 20 concentration data points including 5% of white noise. Data were as follows: (a,c) equisampled in time and (b,d) equisampled in concentration. Simulated data are plotted with symbols; the true and fitted curves are respectively plotted in dotted and solid lines.

5.1. Typical Effect of the Desorption Level on *D*, *K*, and h_m Estimations from Kinetic Data and KPD. The effect of s on fitted desorption kinetics and KPD is illustrated in Figure 5 for $B = 1000$, $K = 0.1$, $L^* = 0.01$, and $s = 50\%$. Uniform sampling in concentration increased the relative weight of initial kinetic data, whereas uniform sampling in time increased the relative weight of data associated to higher desorption rates. Both sampling strategies led apparently to similar fitted kinetics and KPD. However, the $d = 1$ criterion was not able to extrapolate the "real" desorption kinetic beyond $s = 50\%$ without introducing a positive bias. Such an error was responsible for a false prediction of the final equilibrium (almost 0 instead of 0.1) (Figure 5 parts a and b). Despite errors in both u and j^* values, $d \geq 2$ methods led to a better extrapolation of true results for $s > 50\%$. The extrapolated equilibrium value ranged between 0.09 and 0.12 and was furthermore in very good agreement with the true value (Figure 5 parts c and d).

Capabilities of both $d = 1$ and $d = 2$ criteria to estimate D, K, and h_m properties from previous data uniformly sampled in time are compared in Figure 6 from PJCR. Similar results were obtained with data uniformly sampled in concentration. The $d = 1$ method generated a low convex functional with many local minimums and a large confidence ellipsoid that was stretched along h_m and D directions. As a result, only the parameter D could be accurately estimated from kinetic information. By contrast, $d = 2$ generated a hilly functional where the optimal value laid in the bottom of a narrow valley opened toward low D values. Volume of confidence ellipsoid was 5×10^5 lower with $d = 2$ and stretched along the axis (D, $-h_m$). Although K and h_m estimations were highly linear dependent, simultaneous estimations of D, K, and h_m parameters were possible because their respective confidence intervals close to the optimal value were small (Figure 6 parts d and e).

5.2. Effect of *B* and *s* Level on Bias and Confidence on *D*, *K*, and h_m Estimations. The previous analysis was generalized for a wide range of simulated conditions: $B = [10^{-1}, 1, 10, 10^2, 10^3, 10^4] \times K = [10^{-2}, 10^{-1}, 5 \times 10^{-1}, 1, 2, 5] \times L^* = [10^{-3}, 5 \times 10^{-3}, 10^{-2}, 5 \times 10^{-2}, 10^{-1}] \times s = [30, 40, 50, 60,$

L

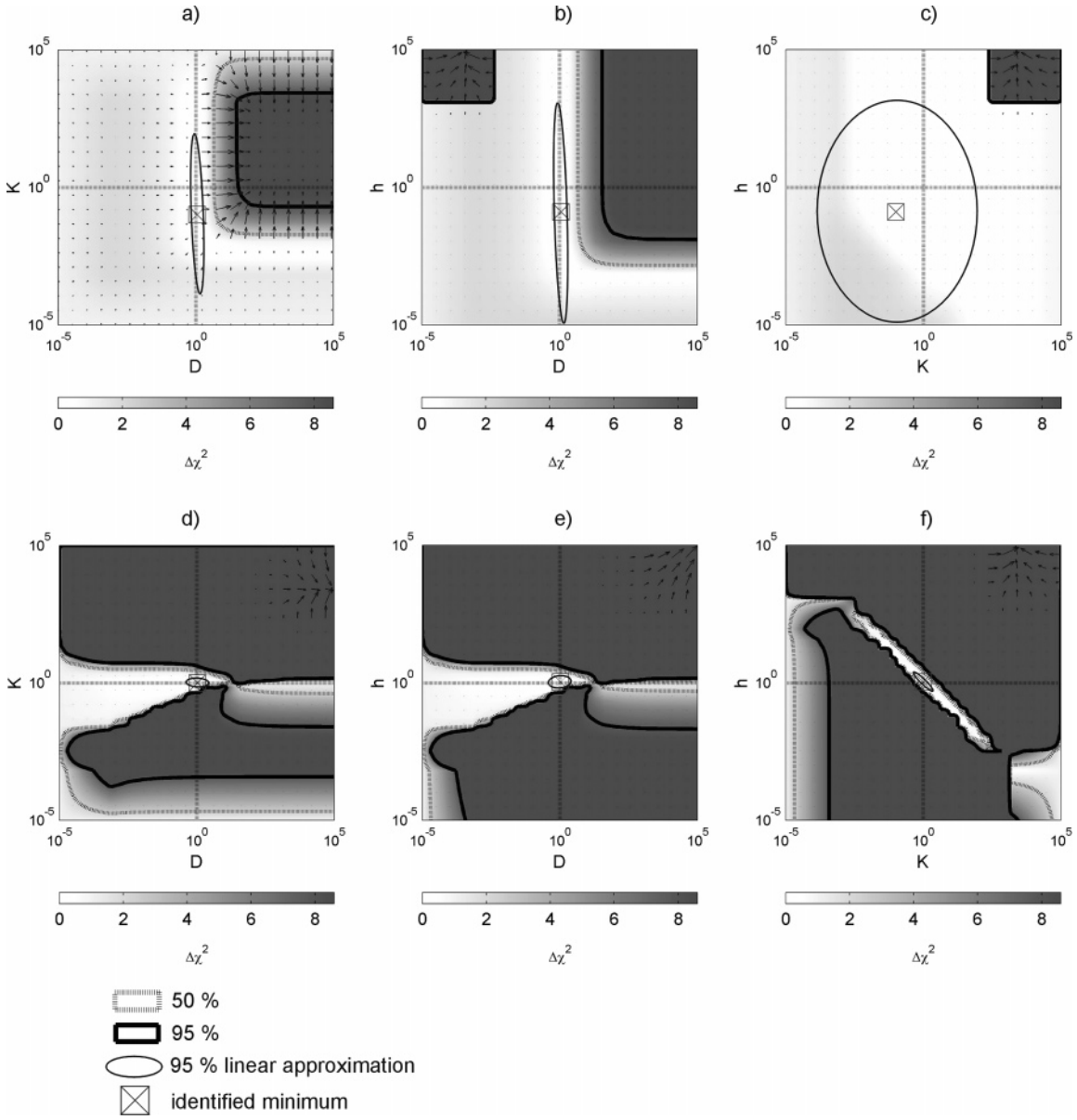

Figure 6. Projected joint confidence regions (PJCR), respectively, to simulated results of Figure 5. PJCR were based on the following: (a,b,c) $d = 1$ and (d,e,f) $d = 2$ criteria. Gray level values represent $\min(\Delta\chi^2, 8)$. The gradient of $\Delta\chi^2$ is superimposed as quiver plots. PJCR based on an approximation of the local information matrix is also indicated. The axes of projections are plotted in dotted lines and correspond to identified values of *D*, *K*, and *h*. The deviation between the identified minimum and the intersection of the projection axis assesses the bias due to the identification procedure.

70, 80, 100] and for both strategies of sampling. Since *B* was the main explicative factor, relative bias and confidence intervals inferred from different (*K*, *L**) values were averaged and compared with *B* only. Results are plotted in Figures 7 and 8 for strategies based on uniform sampling in time and in concentration, respectively. Since $d = 2$ and $d = 3$ criteria had very similar efficiency, only the results for $d = 2$ are given.

For almost all of the tested conditions, approximations of parameters *D*, *K*, and h_m based on $d = 1$ criteria were poor and highly sensitive to *s*. The estimation of *D* was achievable (with a relative bias ~1 unit) for all tested *s* values only when *B* was >100. Accurate estimations of h_m, *K*, and *B* required *s* values higher >70%. These results confirmed that noisy raw kinetic data, which did not include the equilibrium state, were not sufficient for a simultaneous estimation of *D*, *K*, and h_m parameters.

$d = 2$ criteria significantly improved the previous method by making possible low biased and confident estimations of *D*, *K*, and h_m for $B \geq 10$ and *s* values as low as 30%. Both sampling strategies led to similar estimates of tested parameters. Only, the estimation of *B* was slightly improved with a uniform sampling in time by allowing an estimation down to $B = 1$ for $s > 50\%$. It is emphasized that, when no accurate estimation of any parameters *D*, h_m, or *K* was reachable, identification strategies based on $d \geq 2$ generally led to overestimation of the true value of each parameter. By contrast, $d = 1$ strategy could generate either underestimated or overestimated *D* values.

6. Conclusions and Prospects

A robust estimation strategy was proposed to simultaneously identify three properties $p = [D, K, h_m]'$ that control desorption kinetics (or, equivalently, sorption kinetics) under two relevant constraints constraints: low Biot values and incomplete kinetics. The feasibility is demonstrated via a new approximation of 1D diffusion equation coupled with a Robin boundary condition. The approximating differential algebraic equation offers both (i) a very efficient computational alternative to other analytic

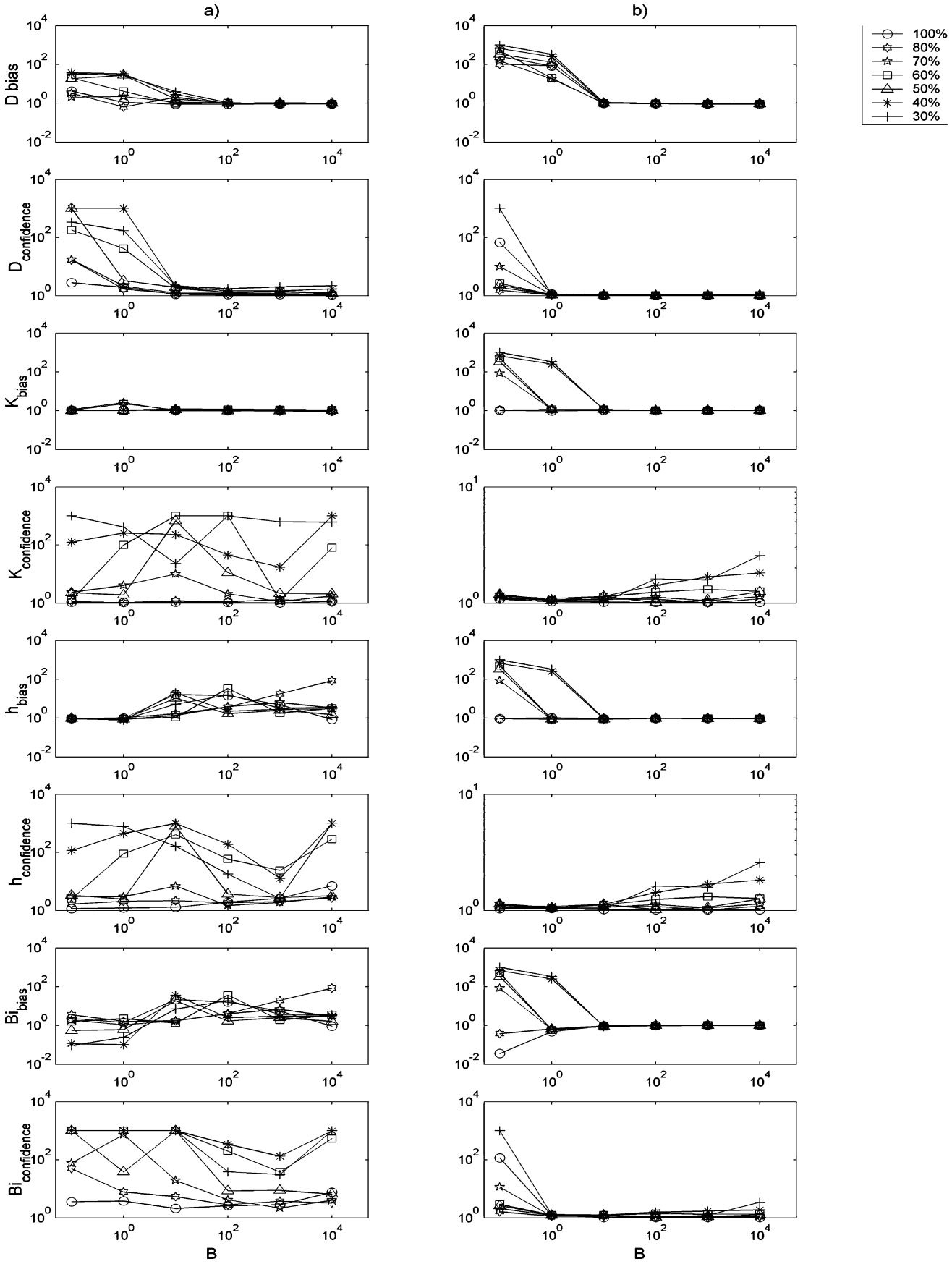

Figure 7. Relative bias and 95% confidence intervals on parameters D, K, h_m, and B estimated from 20 concentration data points equisampled in time and including 5% of noise. The estimations were based on the following: (a) $d = 1$ and (b) $d = 2$ criteria. Data were simulated for different B values, and s values ranged between 30% and 100%. Each depicted point was averaged over 30 simulations corresponding to all combinations of parameters $K = [10^{-2}, 10^{-1}, 5 \times 10^{-1}, 1, 2, 5] \times L^* = [10^{-3}, 5 \times 10^{-3}, 10^{-2}, 5 \times 10^{-2}, 10^{-1}]$.

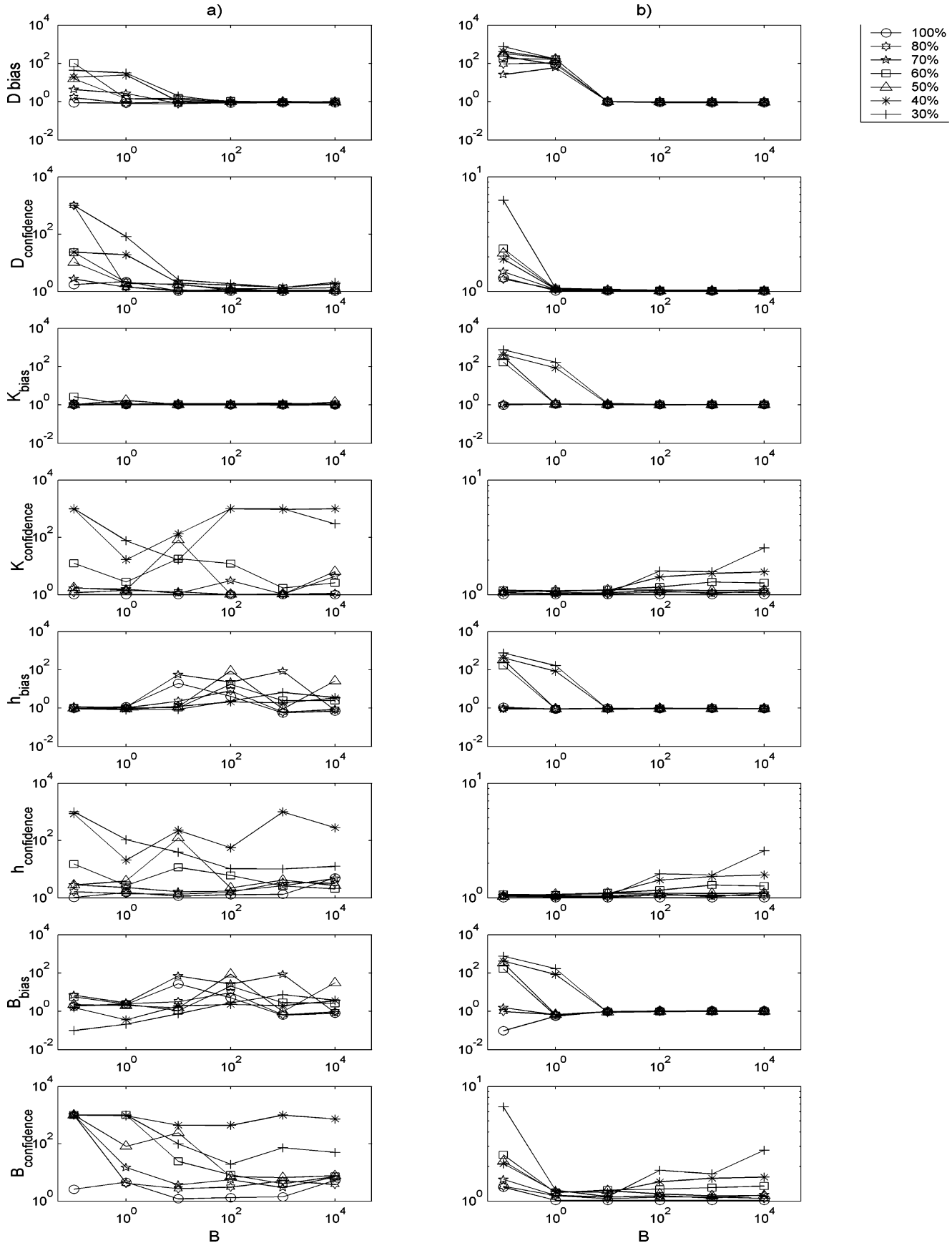

Figure 8. Relative bias and 95% confidence intervals on parameters D, K, h_m, and B estimated from 20 concentration data points equisampled in concentration and including 5% of noise. The estimations were based on the following: (a) $d = 1$ and (b) $d = 2$ criteria. Data were simulated for different B values, and s values ranged between 30% and 100%. Each depicted point was averaged over 30 simulations corresponding to all combinations of parameters $K = [10^{-2}, 10^{-1}, 5 \times 10^{-1}, 1, 2, 5] \times L^* = [10^{-3}, 5 \times 10^{-3}, 10^{-2}, 5 \times 10^{-2}, 10^{-1}]$.

or numeric approximations and (ii) explicit relationships between physical parameters and desorption rates. These features were combined within a generalized least-squares criterion that extends classification techniques by including important physical features such as the scaled mass flux at the solid−fluid interface (j^S) and its variation with the concentration.

Since j^S values were derived from concentration measurements, errors in j^S and concentrations were expected to be partially correlated. The performances according to the number of distance contributions ($d = 1, 2, 3$) were analyzed in terms of bias and confidence on both experimental and simulated data. $d = 1$ strategies led to unreliable estimates of K and h_m for desorption levels < 70%. Besides, it is emphasized that $d = 1$ did not make possible accurate estimations of the mass Biot number. Criteria based on $d \geq 2$ drastically enhanced the accuracy and stability of identification procedure with typical confidence ellipsoid volumes that were reduced by a factor varying between 10^5 and 10^7. These improvements drew the conclusion that the simultaneous identification of D, K, and h_m values and B may be feasible and stable from scattered truncated kinetics for $B \geq 1$ and a wide range of migration conditions: $10^{-2} \leq K \leq 5$, $10^{-3} \leq L^* \leq 10^{-1}$, and desorption levels as low as 30%.

The proposed $d \geq 2$ approach was mainly limited by the information available at the beginning of the migration process when the migration dynamics was the fastest (STC regime). On the basis of kinetics, including 20 points and 5% of white noise, it was, however, shown that the proposed strategy of signal reconstruction of the primitive, first, and second derivatives of the concentration kinetic was almost insensitive to the type of sampling: uniform sampling in either time or concentration. It must be emphasized that the proposed current approach might be used for any migration kinetics to estimate D, K, and h_m parameters or dimensionless quantities such as BK, B, and K/L^* when the cumulative amount of diffusant between both solid and liquid phases remains constant (i.e., without any further mass transfer or reactions). Further works appear desirable to extend results in conditions where boundary conditions vary arbitrarily with time.

Nomenclature

A_i = local regularized regression operator defined in eq 27
B = mass Biot number
b = parameter in eq 16
C_L = bulk concentration in the liquid phase ($kg \cdot m^{-3}$)
C_S = local concentration in the solid phase ($kg \cdot m^{-3}$)
$\overline{C_S}$ = residual concentration in the solid phase ($kg \cdot m^{-3}$)
C_S^0 = initial/typical concentration in the solid phase ($kg \cdot m^{-3}$)
c = parameter in eq 16
d = dimension of the approximation space in eq 28
D = diffusion coefficient ($m^2 \cdot s^{-1}$)
$D_{jl,i}^m$ = mth differentiation operator corresponding to $K_{jl,i}$ (see eq 25)
F = information matrix
K = partition coefficient ($[kg \cdot m_L^{-3}] \cdot [kg \cdot m_P^{-3}]^{-1}$)
$K_{jl,i}$ = collocation matrix corresponding to the ith data (see eq 25)
h = filter bandwidth (s)
h_m = mass transfer coefficient at the S−L interface ($m \cdot s^{-1}$)
J = Jacobian of the model
j = mass flux density at the interface ($kg \cdot m^{-2} \cdot s^{-1}$)
j^* = dimensionless mass flux
j_D^* = equivalent driving flux density in eq 12 ($kg \cdot m^{-2} \cdot s^{-1}$)
j_R^* = equivalent resisting flux density in eq 12 ($kg \cdot m^{-2} \cdot s^{-1}$)
j^S = scaled flux defined in eq 24 ($m \cdot s^{-1}$)
l_L = characteristic length scale of the liquid phase (m)
l_S = characteristic length scale of the solid phase (m)
L^* = dilution factor
M = number of independent data in a data set
m = differentiation order
p = vector of unknown parameters
$\hat{p}$ = estimate of p
R_D = equivalent resistance to diffusion in the P phase ($s \cdot m^{-1}$)
R_H = equivalent interfacial resistance in the L phase ($s \cdot m^{-1}$)
S_{SL} = surface area of the solid−liquid interface (m^2)
s = desorption level
t = time (s)
u = Brownian density or equivalently dimensionless concentration in the solid phase
$\bar{u}$ = dimensionless residual concentration in the solid phase
V_L = volume of the liquid phase (m^3)
v = reduced coordinate defined in Section 2.2.2
X = reduced concentration defined in Section 2.3.3
X_{min} = minimal X value defined in eq 19
x = spatial coordinate (m)
x^* = dimensionless coordinate
x_i^* = dimensionless position of the interface defined in Section 2.2.2
$W_{jl,i}$ = weighting tensor in eq 32

Greek Letters

α = proportionality coefficient defined in eq 12
α^S = scaled value of α used in Section 2.4.2
β = KPD curvature
λ_i = coefficients in eq 28
θ = dimensionless Fourier time
χ^2 = distance function
χ^{2*} = least-squares criterion
σ_X = standard deviation of the quantity X (same unit as X)
ω_{ij} = weighting kernel in eq 26
ξ^2 = regularization parameter in eq 25

Abbreviations

BC = boundary condition
FDP = fully developed parabolic regime
KPD = kinetic phase diagram
IC = initial condition
ODE = ordinary differential equation
PJCR = projected confidence region
PDE = partial differential equation
STC = short-time contact

Literature Cited

(1) Cussler, E. L. *Diffusion—Mass transfer in fluid systems*, 2nd ed.; Cambridge University Press: Cambridge, U.K., 1999.

(2) Vieth, W. R. *Diffusion in and Through Polymers: Principles and Applications*; Hanser Gardner Publishing: Cincinnati, OH, 2000.

(3) Sagiv, A. Theoretical formulation of the diffusion through a slab—Theory & validation. *J. Membr. Sci.* **2002**, *199*, 125−134.

(4) Cranck, J. *Mathematics of diffusion*, 2nd ed.; Oxford University Press: Oxford, U.K., 1975.

(5) Vergnaud, J. M. *Liquid Transport Process in Polymeric Materials: Modeling and Industrial Applications (Polymer Science and Engineering Series)*; Prentice Hall: Englewood Cliffs, NJ, 1991.

(6) European Commission. EU directive 2002/72/EC relating to plastics materials and articles intended to come into contact with foodstuffs. *O. J.* **1991**, L220 of 15.08.2002, 18.

(7) Vitrac, O.; Hayert, M. Risk assessment of migration from packaging materials into foodstuffs. *AIChE J.* **2005**, *51* (4), 1080−1095.

(8) Pàzman, A. Non linear least squares − uniqueness versus ambiguity. *Math. Oper. Stat.* **1984**, *15*, 323−336.

(9) Kendall, M. G.; Stuart, A. *The advanced theory of statistics*; Griffin: London, 1984; Vol. 2.

(10) Bevington, P. R.; Robinson, D. K. *Data reduction and error analysis for the physical sciences*, 2nd ed.; McGraw-Hill: Boston, MA, 1992.

(11) Garthwaite, P. H.; Jolliffe, I. T.; Jones, B. *Statistical Inference*; Prentice Hall: London, 1995.

(12) Chiou, C. R.; Schmedding, D. W. Partitionning of organic compounds in octanol water systems. *Environ. Sci. Technol.* **1982**, *16*, 4−10.

(13) Trefry, M. G.; Whyte, D. S. Analytical solutions for partitioned diffusion in laminates. I. Initial value with steady Cauchy conditions. *Transp. Porous Media* **1999**, *37*, 93−128.

(14) Trefry, M. G.; Öhman, J.; Davis, G. B. A simple numerical approach for assessing coupled transport processes in partitioning systems. *Appl. Math. Modell.* **2001**, *25*, 479−498.

(15) Gandek, T. P.; Hatton, T. A.; Reid, R. C. Batch extraction with reaction: Phenolic antioxidant migration from polyolefins to water. 1. Theory. *Ind. Eng. Chem. Res.* **1989**, *28*, 1030−1036.

(16) Vergnaud, J. M. Problems encountered for food safety with polymer packages: chemical exchange, recycling. *Adv. Colloid Interface Sci.* **1998**, *78*, 267−297.

(17) Weideman, J. A. C; Reddy. S. C. A Matlab Differentiation Matrix Suite. *ACM TOMS* **2000**, *26*, 465−519.

(18) Eubank, R. L. *Non parametric regression and spline smoothing*, 2nd ed.; Marcel Dekker, Inc.: New York, 1999.

(19) Fan, J.; Gijbels, I. *Local polynomial modeling and its application*; Chapman & Hall: London, 1996.

(20) Tikhonov, A. N.; Arsenin, V. Y. *Solutions of ill posed problems*, *Scripta Series in Mathematics*; John Wiley & Sons: New York, 1977.

(21) Hansen, C. Analysis and Solution of Discrete. Ill. Posed Problems. *Numer. Algorithm* **1994**, *6*, 1−35.

(22) Press, W. H.; Teukolsky, S. A.; Vetterling, W. T. *Numerical recipes in C: The art of scientific computing*; Cambridge University Press: Cambridge, U.K., 1997.

Received for review March 22, 2006
Revised manuscript received August 22, 2006
Accepted August 28, 2006

IE060347W